



HAL
open science

MicrOmega/MASCOT first results

Jean-Pierre Bibring, Cédric Pilorget, Lucie Riu, Vincent Hamm, Rosario Brunetto, Tra-Mi Ho, Ralph Jaumann, Yves Langevin, Aurélie Moussi, François Poulet, et al.

► **To cite this version:**

Jean-Pierre Bibring, Cédric Pilorget, Lucie Riu, Vincent Hamm, Rosario Brunetto, et al.. MicrOmega/MASCOT first results. Planetary and Space Science, 2022, 210, 10.1016/j.pss.2021.105393 . insu-03744503

HAL Id: insu-03744503

<https://insu.hal.science/insu-03744503>

Submitted on 8 Jan 2024

HAL is a multi-disciplinary open access archive for the deposit and dissemination of scientific research documents, whether they are published or not. The documents may come from teaching and research institutions in France or abroad, or from public or private research centers.

L'archive ouverte pluridisciplinaire **HAL**, est destinée au dépôt et à la diffusion de documents scientifiques de niveau recherche, publiés ou non, émanant des établissements d'enseignement et de recherche français ou étrangers, des laboratoires publics ou privés.



Distributed under a Creative Commons Attribution - NonCommercial 4.0 International License

1 **MicrOmega/MASCOT first results**

2 *¹Bibring Jean-Pierre, ¹Pilorget Cédric, ²Riu Lucie, ¹Hamm Vincent, ¹Brunetto Rosario, ³Ho
3 Tra-Mi, ⁴Jaumann Ralph, ¹Langevin Yves, ⁵Moussi Aurélie, ¹Poulet François, ¹Vincendon
4 Mathieu, and the MicrOmega/Mascot team

5 ¹ IAS, Institut d'Astrophysique Spatiale, Université Paris-Saclay / CNRS, Orsay France

6 ² ISAS, Institute for Space and Astronautic Science, Sagamihara, Japan

7 ³ DLR, Institute of Space Systems, Bremen, Germany

8 ⁴ DLR, Institute of Planetary Research, Berlin, Germany

9 ⁵ Centre National d'Etudes Spatiales (CNES), France

10 * Corresponding Author, bibring@ias.u-psud.fr

11

12 **Abstract**

13 MASCOT has been selected to be integrated on board the JAXA Hayabusa2 mission, with a
14 suite of 4 instruments: a camera MASCam, a radiometer MARA, a magnetometer MASMag
15 and MicrOmega, a hyperspectral near infrared microscope, designed to characterize the
16 composition of Ryugu surface materials down their grain scale (25 μm large). A joined article
17 (Ho et al., this issue) describes and gives references to MASCOT design, goals, development
18 and operation, along its cruise, landing and on asteroid phase.

19 MicrOmega has been activated and operated as planned, while demonstrating high instrumental
20 performances. However, its configuration when MASCOT went at rest on Ruygu located
21 MicrOmega line of sight over a deep depression, with Ryugu surface much too far to be
22 illuminated and imaged, precluding a direct characterization.

23 In this paper, we present and discuss MicrOmega operations and outcomes.

24

25 **I. The MicrOmega instrument on-board MASCOT**

26 MicrOmega is a near infrared (NIR) hyperspectral microscope designed to characterize *in situ*
27 the texture and composition of Ryugu surface material (Bibring et al., 2017). The instrument
28 has been implemented on-board the MASCOT lander, developed by DLR and CNES (Ho et al.,
29 2017). MicrOmega spectral range is 0.99-3.6 μm , chosen to enable the identification of most
30 minerals and ices, and to detect potential organic compounds within each $25 \times 25 \mu\text{m}^2$ of the
31 $3.2 \times 3.2 \text{ mm}^2$ field of view (FOV) ($128 \times 128 \text{ pix}^2$). The hyperspectral data (3D (x, y, λ) data
32 cubes) are generated by sequentially illuminating the samples with a monochromatic light, then
33 imaged on a 2D detector cooled by a dedicated cryocooler. The illumination is made under an
34 angle 30° inclined with respect to the normal to the object plane, to avoid specular reflection to
35 enter the detector.

36

37 The measurement is performed through a small sapphire window, set on a metallic protuberance
38 a few centimetres long (Fig. 1). It behaves as a foot for MASCOT after proper setting,
39 eventually following an automated up-righting (see Ho et al., this issue). Per design, the
40 focusing is fine-tuned to the window external surface, to which the sample are supposed to be
41 in contact. Additionally, a small part of the sapphire window ($\sim 10\%$) has been depolished and
42 coated with a thin reflecting layer of chromium on its external side. This part of the field of
43 view is used as an inflight Calibration Target (CT, see Figures 6 and 9) to monitor a potential
44 evolution of the instrument response throughout the mission (pre-flight and in space
45 operations).

46



47

48 *Figure 1: Picture of the MicrOmega / Hayabusa2 instrument. The sapphire window through*
49 *which the measurement is performed is covered here by a small protection cap (on the left).*

50

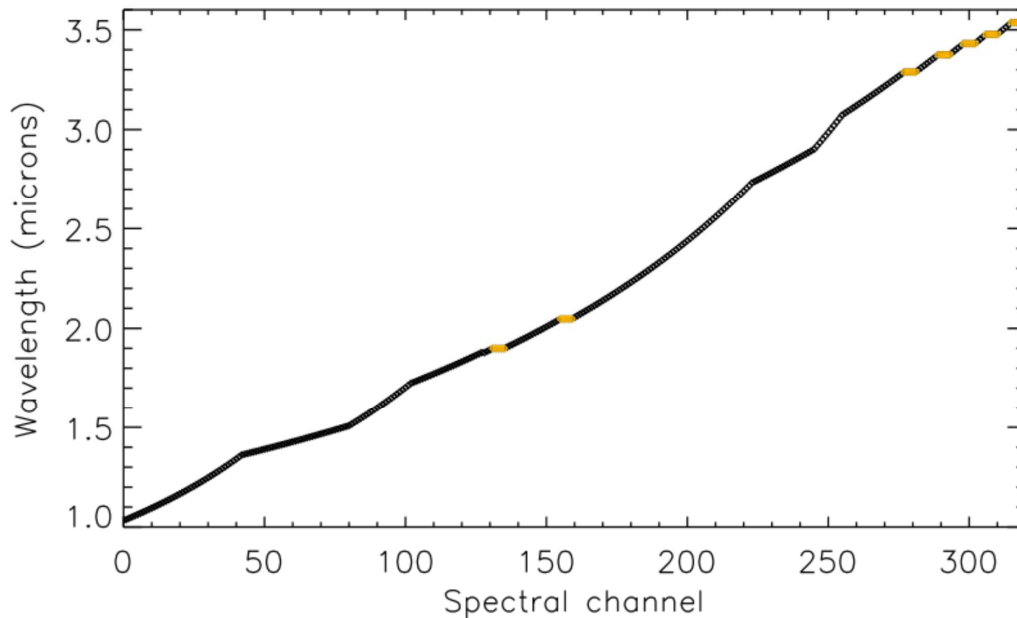
51 The illumination system couples a broadband light source (tungsten lamp) to a monochromator
52 made of an Acousto-Optic Tunable Filter (AOTF) controlled by a radio frequency (RF) signal.
53 Each RF corresponds to a given wavelength of monochromatic output beam. The AOTF has a
54 spectral resolution (FWHM) of 20 cm^{-1} , corresponding to 2 nm at $1.0 \mu\text{m}$ and 24 nm at $3.5 \mu\text{m}$.
55 The capabilities of the RF generator enable to access any wavelength within the $0.99\text{-}3.6 \mu\text{m}$
56 range with down to 2 cm^{-1} sampling steps. MicrOmega can thus acquire any sequence of
57 monochromatic images (MI) *i.e.* with a full flexibility on their number, order and wavelengths.

58

59 For each of the hyperspectral image-cubes, MicrOmega acquires 320 monochromatic images,
60 covering the entire spectral range. The spectral channels and sampling have been chosen in
61 order to optimize the capabilities of the instrument to detect potential absorption features of
62 interest. For some specific wavelengths, the monochromatic images are acquired 5 times in a
63 row in order to maximize the SNR and to provide means to assess the noise level. The
64 distribution of the spectral channels is shown in Figure 2. For each image-cube with 320 spectral

65 channels, a total of 292 different wavelengths are acquired, with seven of them acquired five
66 times in a row (shown in orange in Figure 2).

67



68

69 *Figure 2: Distribution of the spectral channels for each MicrOmega observation on*
70 *MASCOT. The spectral channels indicated in orange corresponds to the spectral channel*
71 *acquired 5 times in a row during the operations.*

72

73 In addition to the monochromatic light, generated by the internal illumination device,
74 scattered/absorbed by the sample and then imaged on the 2D detector, a thermal background
75 coming from both the instrument and the sample does contribute to the signal acquired by the
76 instrument (Bibring et al., 2017; Riu et al., 2018). The dark current has been demonstrated
77 negligible thanks to the use of a cryocooler that cools the detector down 110 K. The AOTF-
78 based illumination system enables to optimize the retrieval of the scientific signal of relevance.
79 In a baselined case, each monochromatic image (MI) is actually the result of the digital
80 accumulation of 16 images with the AOTF ON to which images with the AOTF OFF (thus

81 corresponding to the background) are subtracted. This procedure enables (1) to increase the
82 SNR by summing 16 same images for each wavelength, and (2) to be insensitive to slow
83 variations of the environment since the background is subtracted “on-the-fly”.

84

85 For subsequent processing, each hyperspectral cube is actually composed of 5 sub-cubes of 64
86 monochromatic slices (64 wavelengths acquired in a non-monotonic manner). In addition, the
87 temperatures at various locations within the instrument, including the AOTF, are measured and
88 stored for each image acquisition (see Section III.3).

89

90 **II MicrOmega operation plan**

91 As the operations on Ryugu were supposed to last about 12-15 hours with very limited real time
92 feedback, the entire automated sequence of MASCOT had been defined, tested and loaded on-
93 board MASCOT. As for all instruments, only highly limited possibility to change the
94 acquisitions parameters during the operations were anticipated. MASCOT operational sequence
95 was controlled by an automaton, with triggers determined by either timeouts or sensors outputs,
96 *e.g.* day/night cycle (Ho et al., this issue). Communication to the mother spacecraft, including
97 data transfer, was only possible during Ryugu's day, since the mother spacecraft remained
98 eclipsed during MASCOT local nights.

99

100 Since the uncertainties on the thermal environment of MASCOT and thus of MicrOmega were
101 high, it was chosen to acquire in a row two hyperspectral image-cubes of 320 monochromatic
102 images with 2 different integration times, 5 and 15 ms (referred to as double acquisition

103 hereafter). Single acquisition with only 1 integration was planned for the last phase of the
104 operations, with anticipated low battery load.

105

106 The planned operation sequence thus included:

- 107 • 1 double acquisition during the first day,
- 108 • 1 double acquisition during the first night,
- 109 • A mini-move of MASCOT during the second day, followed by 1 double acquisition,
- 110 • A relocation of MASCOT followed by 1 double acquisition,
- 111 • 1 double acquisition during the second night,
- 112 • 1 double acquisition during the third day,
- 113 • 1 single acquisition.

114

115 **III Operations on Ryugu**

116 **III.1 Overview**

117 MASCOT separation occurred on October 3rd 2018. 6 minutes later, MASCOT reached the
118 surface. After several bounces, MASCOT went at rest. The first data download indicated that
119 the on board system (Ho et al., 2017) to turn MASCOT instruments toward the surface had
120 failed and that MicrOmega as well as MASCam and MARA were facing the sky (Jaumann et
121 al., 2019). Suspecting that a new up-righting would not be necessarily efficient, a relocation
122 was decided, and commanded to be operated as soon as possible, *i.e.* the next local morning.
123 Since all acquisitions sequences were already planned, the first two MicrOmega observations
124 (during the first day and during the first night) were performed with MicrOmega facing the sky.

125 The next local morning (2nd day), the relocation was indeed performed and this time MASCOT
126 could be successfully pointed with MicrOmega window towards the surface. MicrOmega
127 observations have then been performed as scheduled, at first during the day, and then at night.
128 The quick-look feedback obtained from MicrOmega (a few statistics, on-board computed
129 within the signal acquired by the instrument, were successfully transferred in almost real time)
130 revealed that no significant signals were received through the window: it was very likely not in
131 contact with the surface of Ryugu.

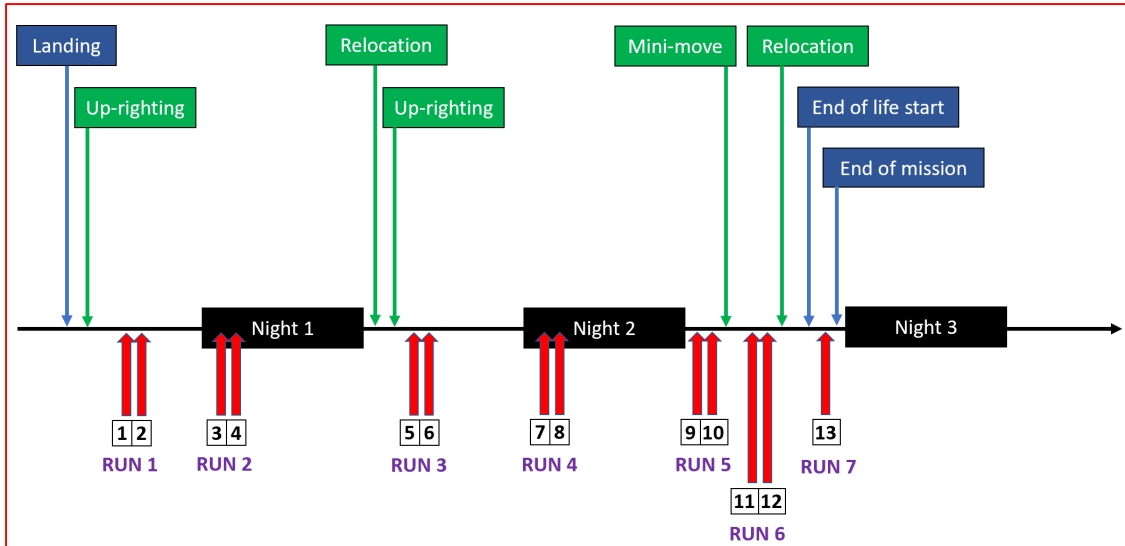
132

133 A mini-move was then commanded with the prime objective to favour the contact between
134 MicrOmega window and the surface. It could only occur in the morning of the 3rd day,
135 unfortunately after a new pre-loaded automated MicrOmega observation. The mini-move
136 successfully occurred. However, as later confirmed by MASCam images, the mini-move had
137 almost no effect on the distance between MicrOmega and the surface (Jaumann et al., 2019). In
138 addition, the environment temperature was then too high, and the detector was saturated by
139 thermal photons.

140

141 A second relocation was then successfully commanded, and a new MicrOmega observation (a
142 single sequence this time) was performed (run 7). Unfortunately, MASCOT ended with
143 MicrOmega facing the Sun, and no up-righting was commanded, given the low battery level.
144 The sequence of events is summarized in Figure 3 and Table 1.

145



146

147 *Figure 3: Summary of the MicrOmega sequences on asteroid Ryugu. The blue boxes indicate*
 148 *the beginning and the end of MASCOT operations. The green boxes correspond to MASCOT*
 149 *manoeuvres listed here above in the text. The red arrows indicate the time of MicrOmega*
 150 *measurements. The number corresponds to each acquired image cubes. Double arrows*
 151 *indicate double image-cubes (5 and 15 ms) and single arrow single image-cube (15 ms).*

152

Run	Time of day	MicrOmega orientation	Location	Image-cubes ID	Status	
					Tint=15ms	Tint=5ms
1	Day	Up	Site 1	Image-cubes 1&2	OK	OK
2	Night	Up	Site 1	Image-cubes 3&4	OK	OK
3	Day	Down	Site 2	Image-cubes 5&6	OK	Saturated
4	Night	Down	Site 2	Image-cubes 7&8	OK	OK
5	Day	Down	Site 2	Image-cubes 9&10	OK	OK
6	Day	Down	Site 3	Image-cubes 11&12	Saturated	Saturated
7	Day	Up	Site 4	Image-cube 13		Power supply was not sufficient

153

154

Table 1: Summary of the MicrOmega measurements on Ryugu.

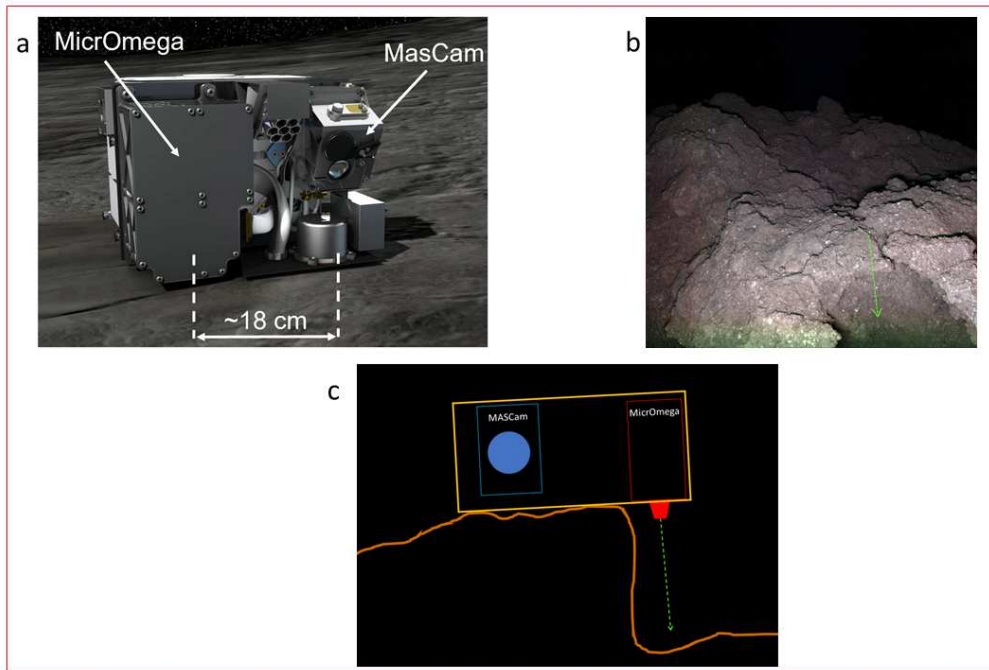
155

156 **III.2 MicrOmega configuration at rest**

157 The post processing of MASCam data by the MASCam team offered a fair representation of
158 the local environment of MicrOmega, accounting for the lack of surface contact of its front
159 window.

160 As seen on MASCam images, MASCOT went at rest in a regolith-free rough area made of
161 boulders a few tens of cm in size. Given the actual location of MicrOmega and MASCam within
162 MASCOT (Figure 4a), MicrOmega FOV is shifted by ~18 cm with respect to MASCam
163 boresight. As a consequence, the MicrOmega field of view was pointing at a depression (Figure
164 4b), which can be evaluated from the MASCam team analyses around 15 to 30 cm distant
165 (Jaumann et al. 2019). This depression below the front window, given its depth, totally
166 precluded surface observations. Per its design as a microscope, the samples were supposed to
167 be in contact with MicrOmega front window to be in focus, or at distances < 5 mm to be
168 illuminated with the monochromatic beam from MicrOmega. The illuminated spot of an object
169 farther away from the window was out of the detector field of view (FOV).

170



171

172 *Figure 4: (a) 3D representation of MASCOT. The boresight direction of MASCam and*
 173 *MicrOmega are about 18 cm apart. (b) MASCam night image on Site 2 (Jaumann et al.,*
 174 *2019) MicrOmega FOV lies within the cavity that can be observed at the bottom right corner*
 175 *(green arrow). (c) illustrating sketch of a plausible geometric configuration of MicrOmega*
 176 *viewing direction.*

177

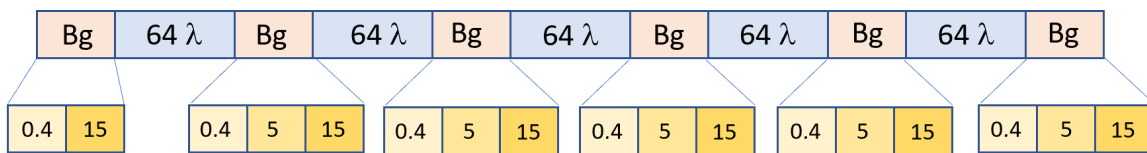
178 **III.3 Context as seen by MicrOmega**

179 For each MicrOmega “double acquisition” observation (corresponding to 2 full hyperspectral
 180 cubes in a row, with 5 and 15 ms integration time), a few background images (with the AOTF
 181 switched off) were acquired and downlinked. Specifically, 3 background images with
 182 integration times of 0.4 ms, 5 ms and 15 ms were acquired every set of 64 monochromatic
 183 images, with in addition 2 background images (with integration times of 0.4 ms and 15 ms)
 184 acquired before the acquisition started (Figure 5). As a consequence, a total of 10 subsets of 64
 185 monochromatic images and 32 background images were acquired for each double acquisition.
 186 These background images were planned to check the quality of the monochromatic images, in
 187 particular when eventually saturated: their on-the-fly subtraction could lead to biased

188 downlinked image-cube. They would also enable to monitor the evolution of the environment
 189 temperature (of both the instrument and the scene) and/or the potential presence of straylight
 190 (*e.g.* from the Sun, either direct or diffused), and *in fine* to reconstruct the sequence of
 191 events/environments as seen by MicrOmega. In a nominal (per design) case, straylight should
 192 not be present as the sample would contact and cover the entire MicrOmega window. However,
 193 during the operations on Ryugu, the instrument was either facing the sky (with no sample) or
 194 facing the surface, but at a large distance: straylight could possibly enter the instrument, as it
 195 has indeed been observed in operation, in specific configurations and times.

196

1 MicrOmega datacube



197

198 *Figure 5. Acquisition sequence within a single MicrOmega hyperspectral cube. Background*
 199 *(Bg) acquisitions at different integration times (0.4, 5 and 15 ms, except the first one which only*
 200 *has 0.4 and 15 ms) are performed between two subcubes of 64 spectral channels. For a single*
 201 *MicrOmega hyperspectral cube, there are thus a total of 17 background images. In the case of*
 202 *a "double acquisition", the sequence keeps the same logic: after the acquisition of the 5th*
 203 *subcube, the sequence continues with the background acquisitions at 0.4, 5 and 15 ms, and then*
 204 *the 1st subcube of the 2nd hyperspectral cube. For a "double acquisition", there are thus a total*
 205 *of 32 background images.*

206

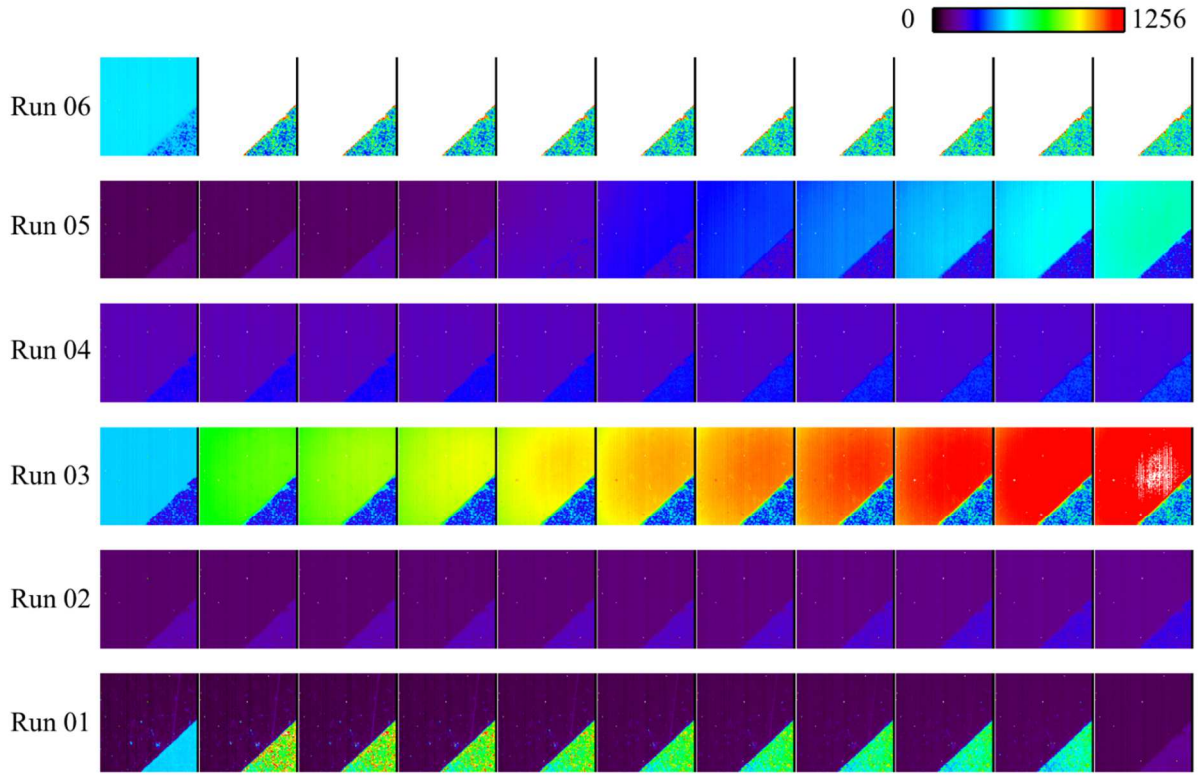
207 From the background images acquired at various integration times (see Fig. 5), a “background
 208 flux” in ADU/s and its evolution could be computed throughout the acquisition sequence.
 209 Figure 6 shows the evolution of the background flux acquired at 5 ms over the MicrOmega field
 210 of view (FOV) for the different observations (clear part and calibration target). Depending on
 211 location/orientation of MicrOmega, we can observe variation in time of the background signal
 212 on the clear part of the FOV.

213 Such background signal observed by MicrOmega was modelled in Riu et al., 2018 (see equation
214 2 in Riu et al., 2018), and is mainly composed of two variable contributions: the thermal
215 emission of the instrument and the thermal emission of the scene (sample) seen by the
216 instrument. In the case where the instrument is not in contact with the surface, a straylight
217 contribution, not taken into account in the model, can also be present. For example, large scale
218 non uniform features with higher or lower background signal are interpreted by the presence of
219 straylight (e.g. run 3 and run 5).

220

221 The temperature of the instrument was monitored by Pt thermal sensors for each image
222 acquisition (Figure 7). Data from these sensors show that MicrOmega encountered large
223 temperature variations on Ryugu (from $\sim 0^{\circ}\text{C}$ at the beginning of Run 1 up to $\sim 40^{\circ}\text{C}$ at the end
224 of Run 4, see Figure 7), sometime close to the maximum operational temperature [-40° , $+40^{\circ}\text{C}$]
225 (Bibring et al., 2017), and performed nominally. The temperature of the instrument increases
226 during an image-cube acquisition since the instrument is per design insulated from the
227 MASCOT lander and has very limited means to dissipate the power of its functioning. Thus, a
228 decrease in the background signal indicates a decrease in the temperature of the scene and/or a
229 change in the contribution of potential straylight. The evolution of the background signal can
230 be different over the on-board calibration target (CT) and on the clear part of the FOV, since
231 this CT is thermally coupled to the structure of the MicrOmega instrument.

232



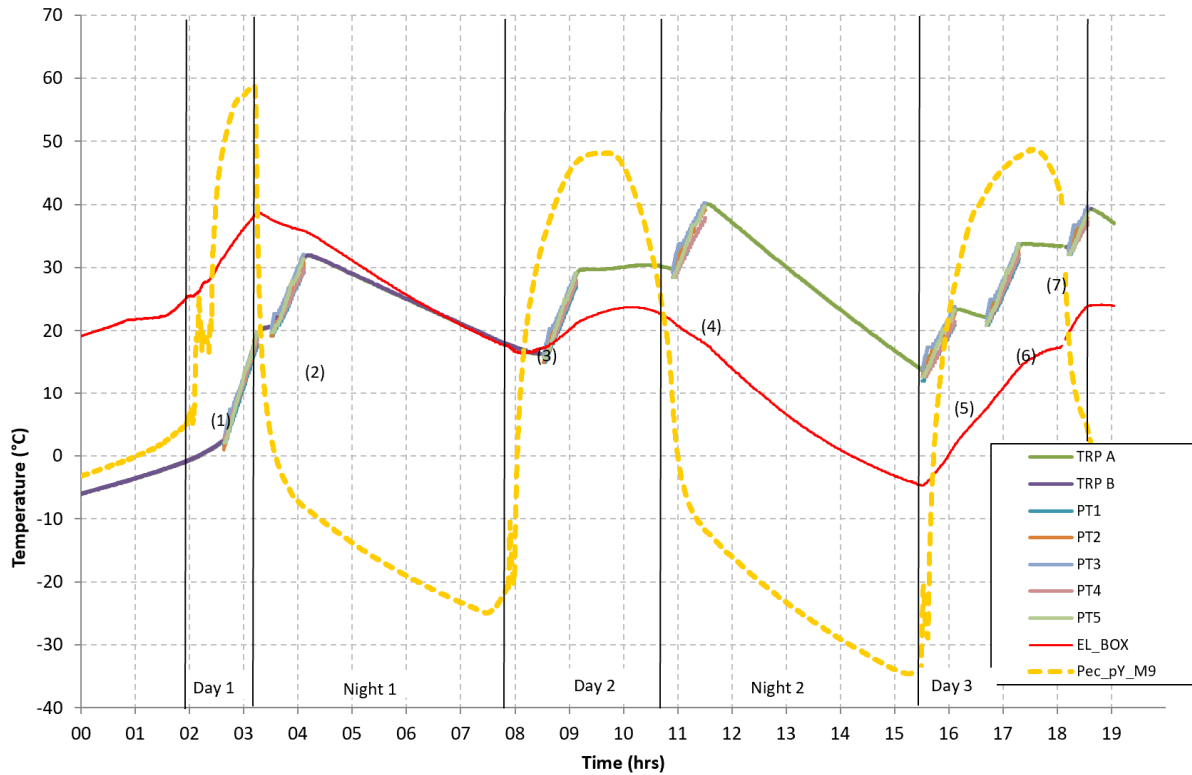
233

234 *Figure 6: Evolution of the background signal (with AOTF OFF) for each of the 6 first runs*
 235 *(see table 1). There are 11 background acquisitions per run acquired throughout the complete*
 236 *acquisition sequence (Figure 3). The background signal in ADU is obtained using*
 237 *background images acquired at 5 ms. Saturated data are shown in white. The variability of*
 238 *signal within the calibration target is due to its heterogeneity at the MicrOmega scale.*

239

240

241



242

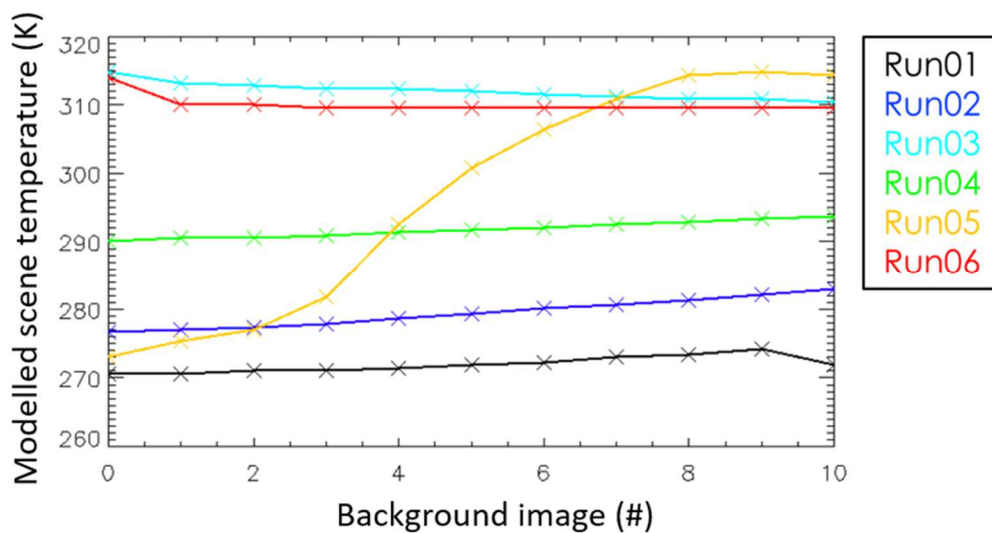
243 *Figure 7: Temperatures as measured by the thermal sensors within the MicrOmega*
 244 *instrument (PT1, PT2, PT3, PT4, PT5), within MicrOmega electronic box (EL_BOX), and at*
 245 *the interfaces with MASCOT (TRP A and TRP B). The signal measured by the sun sensor*
 246 *located on Y panel is also displayed in yellow dashed line.*

247

248 With the temperature data from the Pt sensors, one can model the thermal emission of the
 249 instrument and estimate the remaining background contribution summing the thermal emission
 250 of the scene and some possible additional straylight. This background contribution is hereafter
 251 simplified as a thermal emission of the imaged scene at a temperature T , shown in Figure 8. We
 252 observe that such a temperature is increasing with time for the runs 1 (image-cubes 1&2), 2
 253 (image-cubes 3&4), 4 (image-cubes 7&8) and 5 (image-cubes 9&10) and decreasing for the
 254 runs 3 (image-cubes 5&6) and 6 (image-cubes 11&12). The runs 3 and 6, for which a decrease
 255 of the background signal is observed, occurred during the day which suggests that the imaged
 256 scene might have gone from sun to shadow during both measurements or that the measurements
 257 were acquired after the actual local noon (when the surface temperature supposedly starts

258 decreasing) until dawn (cf Figure 1 in Hamm et al., 2019). For the other measurements, we
 259 observe an increase of the signal for both daytime (run 1 & run 5) and night-time (run 2 & run
 260 4) acquisitions. The temperature is increasing by a few K (up to ~10 K) over one observation
 261 (taking about 32 minutes), except for the run 5 where the temperature increases by more than
 262 40 K. Note that the change in the modelled temperature from the scene are of a few degrees for
 263 most of the runs (except for run 5). The trends can be explained for the different measurement
 264 either by varying straylight entering the detector and/or an increase or decrease of the actual
 265 “scene” temperature. A small difference between the actual and the measured instrument
 266 temperature could explain the differences observed. However, because the instrument
 267 temperature is known to increase during one acquisition, while we observe either a slight
 268 increase (runs 1, 2 and 4) or a slight decrease (runs 3 and 6), we are confident that these
 269 modelled temperatures do not translate that of the instrument.

270



271

272 *Figure 8: Estimated “scene temperature” based on the background signal contribution. The*
 273 *temperature of the scene is estimated on the complete FOV (average of the background signal*
 274 *on all pixels) excluding the calibration target. The “scene” emissivity is set to 1. Each cross*
 275 *corresponds to one background image. The background images are acquired sequentially*
 276 *(i.e., background image #0 is acquired first and background image #10 is last) over the*
 277 *corresponding run.*

278

279 For the measurements where MicrOmega is facing the sky, the increase of background signal
280 from the scene, assuming that the instrument temperature is well-retrieved with the Pt sensors,
281 most likely translates an increase of the direct solar illumination reaching the detector (run 1 &
282 run 2).

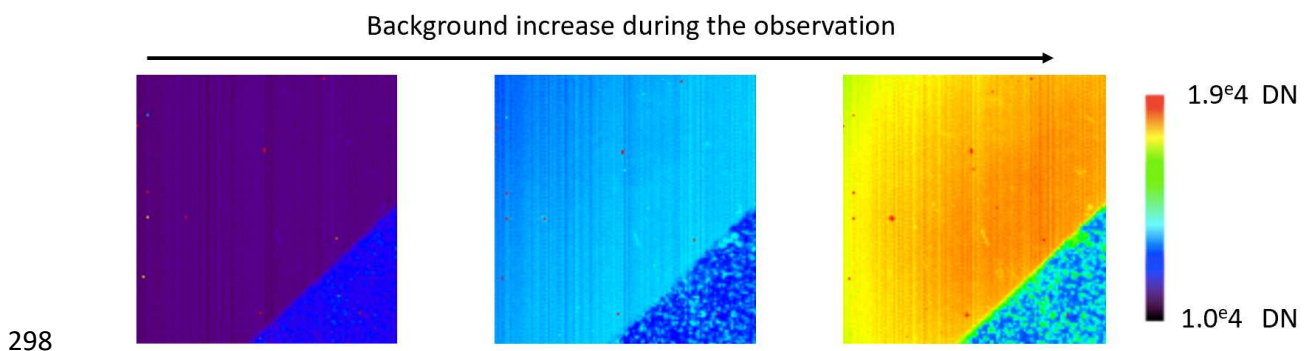
283

284 For the measurements where MicrOmega is facing the surface, an increase in temperature could
285 translate that (1) the imaged surface is heated by the sun and/or by MASCOT itself, and/or (2)
286 some solar straylight (possibly diffused from the surface) is reaching the detector. For the run
287 5, the increase in temperature is very different from the other observations. The measurement
288 lasted ~30 minutes, which would mean that Ryugu's surface is heating up faster than 1 K per
289 minute during the overall measurement, if we exclude straylight. The presence of a large scale
290 heterogeneity in the background signal observed over the FOV (Figure 9) suggests the presence
291 of straylight and/or a quick rise of the temperature of the area that MicrOmega is facing.

292

293 This agrees with the conclusion made on the configuration of MicrOmega: very unfortunately,
294 at the location MASCOT went to rest after relocation and up righting, MicrOmega front
295 window was facing a tens of cm distant surface instead of being in contact or at least close
296 enough (< 5 mm) to be able to image it, after proper monochromatic illumination.

297



299 *Figure 9: Background signal evolution during Run 05. The vertical pattern corresponds to a*
300 *variation of the detector's column response. The large-scale smooth evolution of the*
301 *background signal (typically increasing from left to right), unseen in the calibration results,*
302 *tends to suggest either some straylight or a background environment with a thermal gradient.*

303

304 **IV Data analysis**

305 **IV.1 Calibration process**

306 The transfer function of the instrument has been derived, through on-ground calibration tests,
307 as a function of the RF frequency applied to the AOTF, the temperature of the instrument and
308 the position of the pixel within the FOV (Riu et al., 2018). The wavelength of the light spectrally
309 filtered by the AOTF is driven by the RF frequency through a bijective relation, determined
310 during the on-ground calibration (Riu et al., 2018).

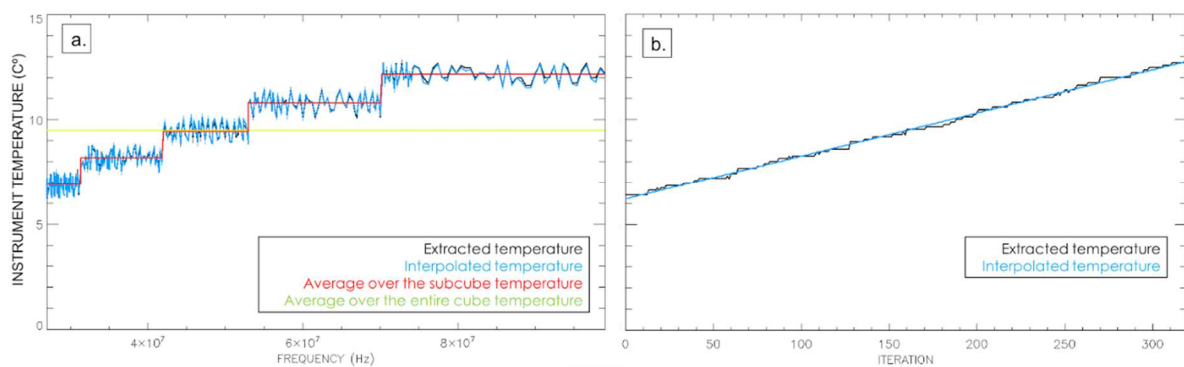
311

312 Within the 13 hyperspectral cubes acquired on Ryugu, we observe that the instrument
313 temperature during the acquisition of one sub-cube varies at most by 1.2 K, thus by 6.5 K for
314 the acquisition of the complete hyperspectral cube (320 wavelengths, 5 sub-cubes). The fact
315 that, for each sub-cube, the wavelengths are not acquired in a monotonic manner (thus between
316 two contiguous wavelengths the temperature may have varied by up to 1.2 K) may create
317 potential artefacts if the temperature variations are not taken into account. We therefore tested
318 different ways to build the most reliable transfer function, and to quantify their potential biases:

- 319 • using the exact extracted instrument temperature for each monochromatic image: total
320 of 320 different measured temperatures to build the transfer function (black line on
321 Figure 10 a & b)
- 322 • using an interpolated instrument temperature for each monochromatic image, based on
323 the hypothesis that the instrument temperature should increase smoothly throughout the

- 324 overall measurement time: total of 320 different interpolated temperatures to build the
- 325 transfer function (blue line on Figure 10 a & b)
- 326 • using an average temperature for each sub-cube: total of 5 different temperatures to
- 327 build the transfer function (red line on Figure 10 a)
- 328 • using only one average temperature over the complete spectral range: 1 temperature to
- 329 build the transfer function (green line on 10 a)

330



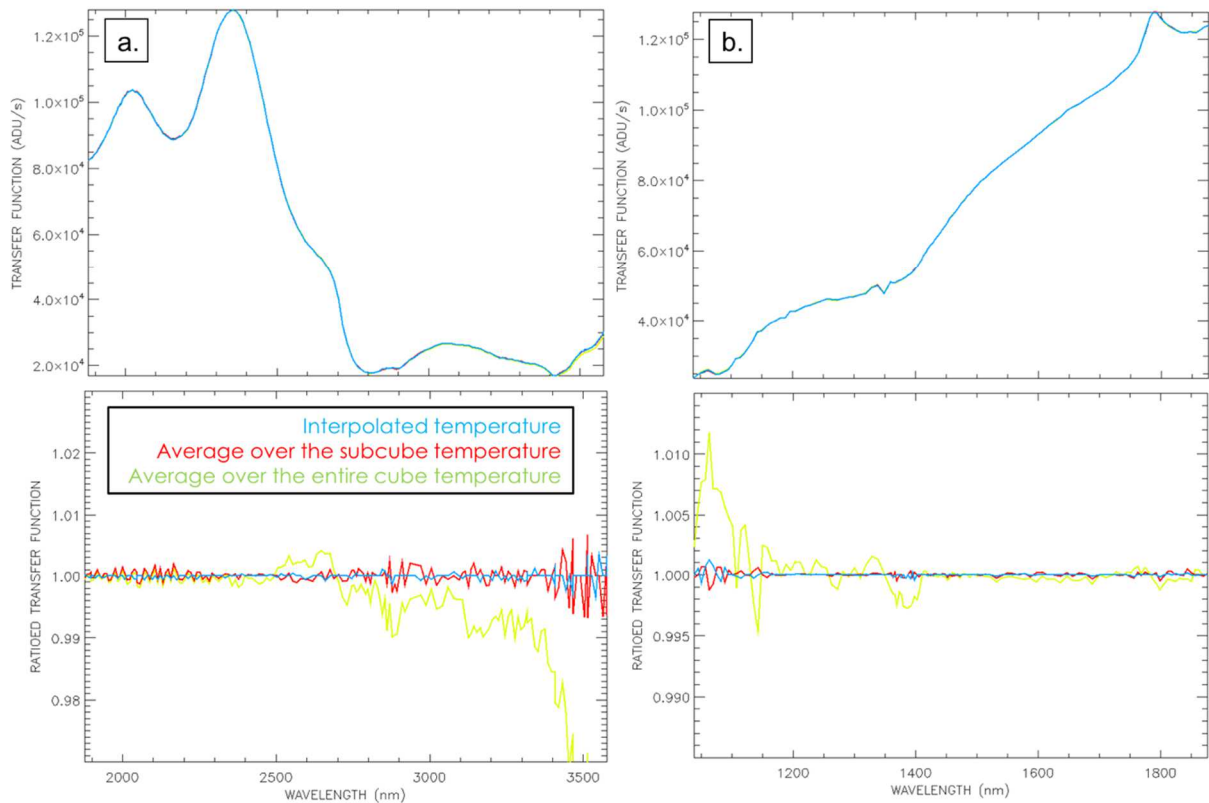
331

332 *Figure 10: (a) Evolution of the instrument temperature with respect to the frequency of the*

333 *AOTF. Each plateau corresponds to a sub-cube. (b) Evolution of the temperature with respect*

334 *to time.*

335



336

337 *Figure 11: Evaluation of the transfer function with respect to the wavelength for both (a)*
 338 *channel 1 (low frequencies/high wavelengths) and (b) channel 2 (high frequencies/low*
 339 *wavelengths). The final transfer function is represented in light blue. The different curves*
 340 *overlap. The bottom part represents the transfer function ratioed with respect to the “actual”*
 341 *temperature transfer function (black line on Figure 7).*

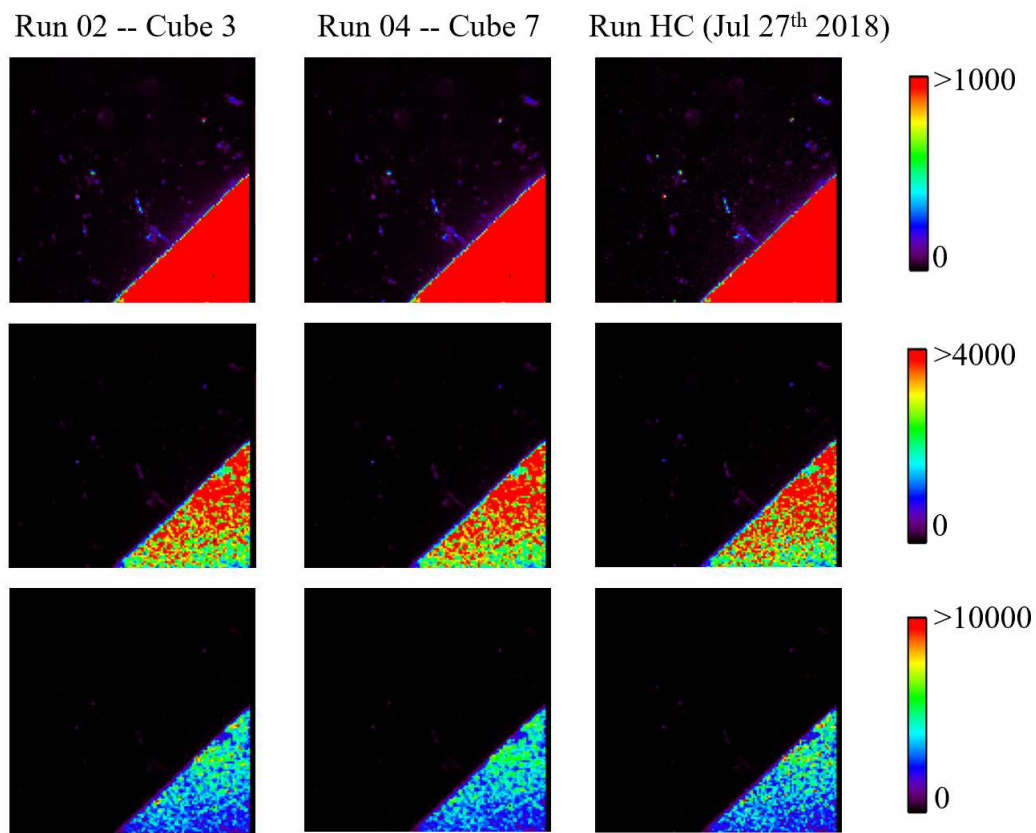
342

343 The different transfer functions differ by less than 1% over the MicrOmega spectral range
 344 except for the transfer function computed with a single temperature averaged on the overall
 345 measurement, which at low frequency (*i.e.*, long wavelength) differs by a few percent. The
 346 slight differences between the other processing do not have a significant impact on the
 347 calibrated spectra. On what follows, we applied the transfer function that uses interpolated
 348 temperatures because it best reflects the evolution of the instrument’s temperature (blue one in
 349 Figure 10 and Figure 11).

350

351 **IV.2 Data analysis**

352 When MicrOmega is actually facing Ryugu's surface, no large sample/grains can be observed
353 in MicrOmega images (Figure 12 left). As quoted above (III.2), the surface of MicrOmega
354 along its boresight is too far (>15 cm) to be illuminated by the monochromatic light emitted by
355 the instrument although MicrOmega window is set on a small metallic cone behaving as a foot
356 for MASCOT, designed to enhance the probability to be in contact with the surface.



357

358 *Figure 12: Background subtracted images acquired at 48.4 MHz (2.05 μm) for various runs.*
359 *The scale is changed from bottom to top to enhance the contrast on the images. Left: Run 02,*
360 *image-cube 3. Center: Run 04, image-cube 7. Right: Health Check on July 27th 2018. The*
361 *Health Check data have been scaled to account for a different integration time.*

362

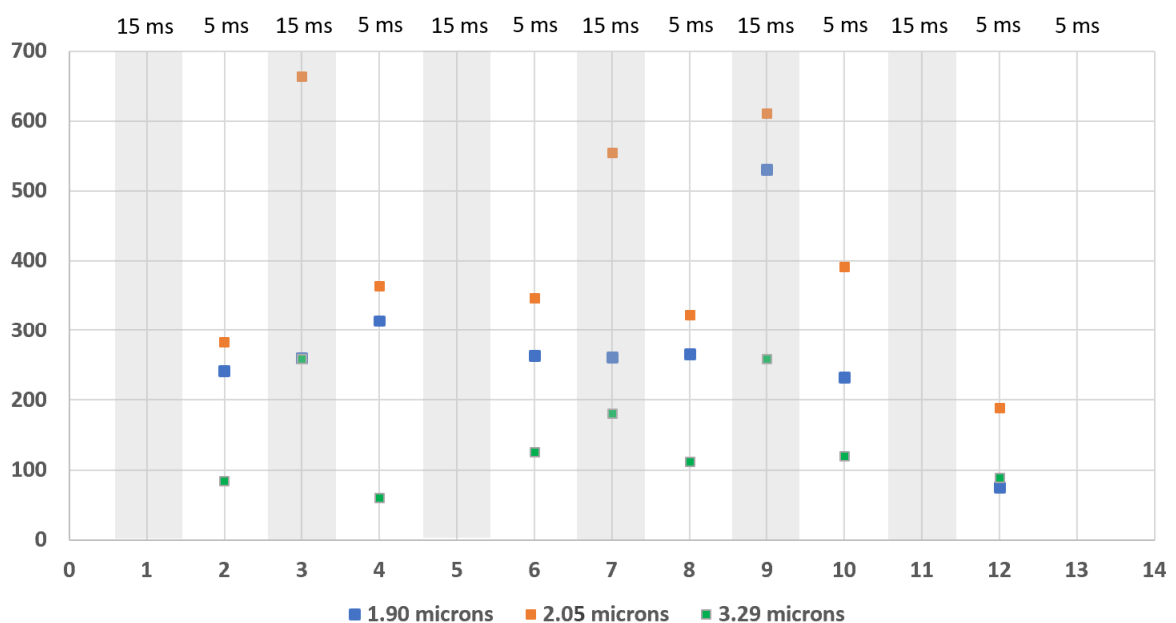
363 When increasing the contrast, some small structures can be detected on the MicrOmega
364 window. A comparison with the data acquired during Health Checks prior to the on-asteroid

365 operations (*i.e.*, while still attached to the Hayabusa2 spacecraft) showed (Figure 12 right) that
366 such small structures were actually present. This was not considered as putting the
367 measurements at risk, when superimposed on the surface in contact. They show up with
368 enhanced contrast only because of the lack of contact surface. They translate the high
369 performances of MicrOmega, both in image and spectral quality, and sensitivity.

370

371 The Signal to Noise Ratio (SNR) was measured during the on-asteroid operations using a few
372 wavelengths for which the images were acquired 5 times in a row. Actually, the SNR has shown
373 to be very high (see Figure 13), consistently with the on-ground calibration results (Riu et al.,
374 2018). Typical values of a few hundreds have been measured at a single pixel scale over the
375 calibration target which has a typical albedo of ~10-15%. The SNR variations that can be
376 observed from one observation to the next are both linked to the evolution of the background
377 signal (thermal emission from the instrument/the surface and eventual straylight from the sun)
378 and to the integration time (both are displayed on Figure 13 for comparison).

379



380

381 *Figure 13: SNR at the pixel scale as measured by MicrOmega on the calibration target*
382 *during the on asteroid operations (x-axis represent the different hyperspectral cubes acquired*
383 *at the surface of Ryugu). The SNR is here computed as the ratio of the mean value to the*
384 *standard deviation.*

385

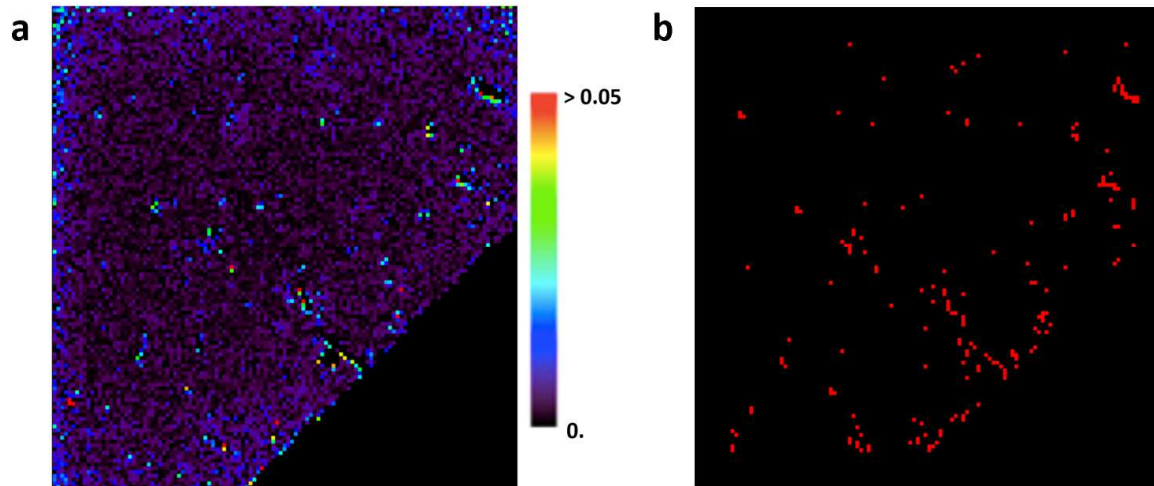
386 The central question for us was thus: would not have MASCOT, before getting to rest,
387 intercepted a few Ryugu “floating” grains, possibly ejected upon collisions, or during
388 relocation, with some eventually collected onto MicrOmega window? In other words, would
389 not at least some of the small structures detected on the clear part of MicrOmega window
390 originate from Ryugu, enabling to identify their composition? At even a much smaller, subpixel,
391 scale, would not Ryugu compounds be spread as an unresolved “background” material? This
392 is the direction to which most efforts were targeted. Each hyperspectral cube acquired after
393 landing was thus scrutinized and a list of pixels where the signal was significantly different
394 from that of the Health Checks has been established (e.g. Figure 14).

395

396 Most runs were not as useful as hoped. Run 6 (corresponding to the 11th and 12th full
397 hyperspectral cubes) was the next observation after MASCOT mini-move (the mini-move
398 should have been performed just when the surface temperature was still relatively cold, as a run
399 5, but the command sent from ground could not be timely received by MASCOT and thus was
400 executed as run 6. Therefore, although MicrOmega temperature was still around 30°C, the local
401 time was around noon and the background signal was too high for the integration times that had
402 been selected. The detector was, thus, saturated and no useful data could be retrieved. Run 7
403 (corresponding to the 13th full hyperspectral cube) was performed after a complete relocation.
404 Unfortunately, the battery load was already too low and the power supply had dropped,
405 generating huge artefacts in MicrOmega data.

406

407



408

409 *Figure 14: (a) Absolute difference between image-cube 7 (run 4) and the Health Check*
410 *performed in July 2018 at 2.05 microns. The difference displayed here corresponds to the*
411 *mean difference over 5 consecutive monochromatic images acquired at 2.05 microns. (b) Map*
412 *of pixels where the difference displayed in (a) is above 1% (a band of 10 pixels has been*
413 *removed on each side to remove noisy data).*

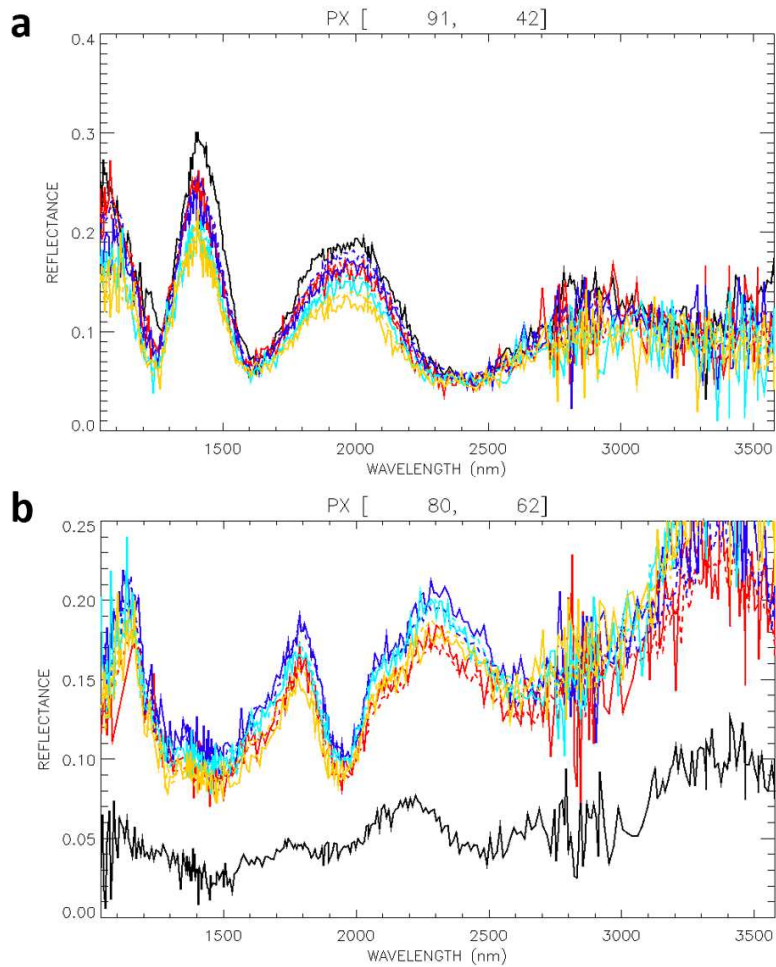
414

415 Systematic studies were conducted to try account for the difference between the response
416 prior and after landing (14b), as to track potential grains from Ryugu that might have got stuck
417 on the window. We also evaluated their “thermal” response based on the background images.
418 We took into consideration all hyperspectral data acquired on Ryugu for our analysis and
419 compared them with data from the Health Checks. Results have shown that the spectral shape
420 of these pixels was constant throughout the complete on-asteroid operations (Figure 15),
421 indicating that if a few grains from the asteroid got stuck on the window, it happened during
422 the first bouncing stage before the settlement, right before the beginning of the observations
423 (run 1).

424

425 Amongst the potential candidates, some tend to display a spectrum of shape similar to that
426 acquired during the Health Checks, but with a higher albedo. This albedo is generally much
427 higher than what was observed from orbit (Kitazato et al., 2019), which can be expected at grain
428 scale (at least for some grains). The presence of inclusions with higher albedo at the microscopic
429 level is observed in chondrites (Cloutis et al., 2011) and MASCam observations have also
430 revealed some heterogeneities at the mm/cm scale (Jaumann et al., 2019). The potential
431 presence of small grains with 10-20% albedo on the window thus cannot be ruled out. However,
432 the dominant spectral features seem to originate from photometric effects like interferences
433 (Figure 15), driven by the subpixel scale of the structures, preventing an unambiguous retrieval
434 of diagnostic compositional spectral characteristics.

435



436

437 *Figure 15: Examples of pixel spectra obtained during Health Check (in black) and operations*
 438 *on Ryugu (in color) displaying interferences. For some occurrences, the signal remains the*
 439 *same as during the Health Check (a), while for some others differences can be observed (b).*

440

441 **V Conclusion**

442 Launched in December 2014, Hayabusa2 reached its target Ryugu, a near Earth C-type asteroid
 443 of less than 1 km in size, after a cruise of 3.5 years during which MicrOmega has been regularly
 444 activated for Health Checks and to get prepared for operations. MASCOT was released on
 445 October 3rd 2018, for an on-asteroid sequence of operations of ~17 hours. During this period,
 446 MicrOmega has been activated 7 times and has acquired 13 full hyperspectral cubes, for a total
 447 duration of activity of 244 minutes, generating 143 Mbytes of data, all received on Earth.

448 MicrOmega operated as planned, and demonstrated a high level of performances, never
449 achieved for an *in situ* microscopic mineralogical and molecular compositional
450 characterization. However, no one had envisioned that the target asteroid would bear a regolith-
451 free boulder-based surface structure, and that the random trajectory of MASCOT would end in
452 such an unfortunate configuration, with MicrOmega line of sight over a depression precluding
453 a microscopic characterization of its surface. Would MicrOmega front window be in contact
454 with, or at millimetres distance from Ryugu surface, its structure and heterogeneous
455 composition, down its 25 μm spatial sampling, would likely have been straightforwardly
456 characterized. The possibility that MicrOmega window has collected some Ryugu grains during
457 bouncing is however still opened, and requires more investigation to be performed.

458

459 The profound frustration could be rapidly compensated, as a similar MicrOmega instrument is
460 now implemented within the Hayabusa2 Curation Facility at

461

462 the Extraterrestrial Samples Curation Center of JAXA (Japan Aerospace Exploration Agency), at ISAS
463 (Institute of Space and Astronautical Science) in Sagamihara. It is performing a preliminary Near
464 InfraRed characterization of the entire collection of the samples collected at Ryugu surface,
465 returned to Earth in December, 2020. A dramatic challenge, with utmost promises, still stands
466 ahead of us.

467

468 **References**

469 Bibring, J.-P., Hamm, V., Langevin, Y., Pilorget, C., Arondel, A., Bouzit, M., Chaigneau, M.,
470 Crane, B., Darié, A., Evesque, C., Hansotte, J., Gardien, V., Gonnod, L., Leclech, J.-
471 C., Meslier, L., Redon, T., Tamiatto, C., Tosti, S., & Thoeres, N. (2017). The

- 472 MicrOmega Investigation Onboard Hayabusa2. *Space Science Reviews*, 208(1–4),
473 401–412. <https://doi.org/10.1007/s11214-017-0335-y>
474
- 475 Cloutis, E.A, Hudon, P., Hiroi, T., Gaffey, M.J., Mann, P., 2011. Spectral reflectance
476 properties of carbonaceous chondrites: 2. CM chondrite. *Icarus* 216, 309-346.
477 doi:10.1016/j.icarus.2011.09.009
- 478
- 479 Hamm, M., Grott, M., Kührt, E., Pelivan, I., Knollenberg, J., 2018. A method to derive
480 surface thermophysical properties of asteroid (162173) Ryugu (1999JU3) from in-situ
481 surface brightness temperature measurements. *Planetary and Space Science*, 159, 1-10.
482 <https://doi.org/10.1016/j.pss.2018.03.017>
483
- 484 Ho T-M., V. Baturkin, R. Findlay, C. Grimm, J.T. Grundmann, C. Hobbie, E. Ksenik, C. Lange,
485 K. Sasaki, M. Schlotterer, M. Talapina, N. Termtanasombat, E. Wejmo, L. Witte, M.
486 Wrasmann, G. Wübbels, J. Röbber, C. Ziach, J. Biele, C. Krause, S. Ulamec, M. Lange,
487 O. Mierheim, R. Lichtenheldt, M. Meier, J. Reill, H.-J. Sedlmayr, P. Bousquet, A.
488 Bellion, O. Bompis, C. Cenac-Morthe, M. Deleuze, S. Fredon, E. Jurado, E. Canalias,
489 R. Jaumann, J.-P. Bibring, K.H. Glassmeier, M. Grott, L. Celotti, F. Cordero, J.
490 Hendrikse, T. Okada (2017): MASCOT the mobile asteroid surface scout onboard the
491 HAYABUSA2 mission. *Space Science Review*, doi:10.1007/s11214-016-0251-6
- 492 Ho T-M., Ralf Jaumann, Jean-Pierre Bibring, Matthias Grott, Karl-Heinz Glaßmeier, Aurelie
493 Moussi, Christian Krause, Ulrich Auster, Jens Biele, Federico Cordero, Barbara
494 Cozzoni, Clement Dudal, Cinzia Fantinati, Jan-Thimo Grundmann, Maximilian
495 Hamm, David Hercik, Kağan Kayal, Joerg Knollenberg, Oliver Küchemann, Caroline
496 Lange, Michael Lange, Laurence Lorda, Michael Maibaum, Yuya Mimasu, Celine
497 Cenac-Morthe, Tatsuaki Okada, Cedric Pilorget, Josef Reill, Takano Saiki, Kaname
498 Sasaki, Markus Schlotterer, Nicole Schmitz, Nawarat Termtanasombat, Nortbert Toth,
499 Yuichi Tsuda, Stephan Ulamec, Friederike Wolff, Tetsuo Yoshimitsu, Christan Ziach
500 and the MASCOT Team (2020): **The MASCOT lander aboard Hayabusa2: The in-**
501 **situ exploration of NEA (162173) Ryugu, this issue**
502
- 503 Jaumann, R., Schmitz, N., Ho, T.-M., Schröder, S. E., Otto, K. A., Stephan, K., Elgner, S.,
504 Krohn, K., Preusker, F., Scholten, F., Biele, J., Ulamec, S., Krause, C., Sugita, S.,
505 Matz, K.-D., Roatsch, T., Parekh, R., Mottola, S., Grott, M., ... Kouyama, T. (2019).
506 Images from the surface of asteroid Ryugu show rocks similar to carbonaceous
507 chondrite meteorites. *Science*, 365(6455), 817–820, and Supplem. materials.
508 <https://doi.org/10.1126/science.aaw8627>
509
- 510 Kitazato, K., Milliken, R. E., Iwata, T., Abe, M., Ohtake, M., Matsuura, S., Arai, T.,
511 Nakauchi, Y., Nakamura, T., Matsuoka, M., Senshu, H., Hirata, N., Hiroi, T., Pilorget,
512 C., Brunetto, R., Poulet, F., Riu, L., Bibring, J.-P., Takir, D., ... Tsuda, Y. (2019). The
513 surface composition of asteroid 162173 Ryugu from Hayabusa2 near-infrared
514 spectroscopy. *Science*, eaav7432. <https://doi.org/10.1126/science.aav7432>
515
- 516 Riu, L., Bibring, J.-P., Pilorget, C., Poulet, F., & Hamm, V. (2018). The on-ground calibration
517 performances of the hyperspectral microscope MicrOmega for the Hayabusa-2
518 mission. *Planetary and Space Science*, 152, 31–44.
519 <https://doi.org/10.1016/j.pss.2018.01.009>